Chapter   2

PRIMITIVE EQUATION MODEL

2.1   Governing Equations

The model used in this study is admittedly simple, though we believe for the expressed goals it is quite appropriate. Before proceeding, some brief physical considerations regarding the MJO are given to argue the models suitability.

The MJO is normally found in a narrow band about the equator ($\sim 10°$S,$10°$N) so using an equatorial β-plane to approximate this region is very reasonable. The observed horizontal circulation patterns are O($10,000$ km), making the quasi-static approximation well-founded. Latent heating effects due to water vapor in the atmosphere are especially important in the tropics. While they most certainly play an important role in the evolution of this tropical weather system, the essential large scale features, which are of concern here, should be satisfactorily resolved without including a detailed moisture budget, but rather by simply including a specified diabatic heating. Based on these judgements, the equatorial β-plane quasi-static primitive equations are a legitimate theoretical framework. These are listed as the set (2.1)–(2.5),

$$\frac{Du}{Dt} - \beta y v + \frac{1}{\rho}\frac{\partial p}{\partial x} = F_x, \tag{2.1}$$

$$\frac{Dv}{Dt} + \beta y u + \frac{1}{\rho}\frac{\partial p}{\partial y} = F_y, \tag{2.2}$$

$$\frac{1}{\rho}\frac{\partial p}{\partial z} + g = 0, \tag{2.3}$$

$$\frac{\partial \rho}{\partial t} + \nabla \cdot (\rho \mathbf{V}) = 0, \tag{2.4}$$

$$c_p\frac{DT}{Dt} - \frac{1}{\rho}\frac{Dp}{Dt} = \mathcal{D}. \tag{2.5}$$

For a stratified, compressible atmosphere the standard forms of the hydrostatic and continuity equations are given by (2.3) and (2.4) respectively. The horizontal momentum equations (2.1), (2.2) have frictional forcing terms F_x and F_y. The last equation, the first law of thermodynamics, has a forcing term ($\mathcal{D}$) that accounts for all diabatic effects.

For convenvience we choose to use the vertical log-pressure coordinate, $z = \ln(p_0/p)$, where $p_0 = 1010$ hPa is a constant "surface" pressure. Conversion of equations (2.1)–(2.4) to this vertical coordinate is the topic of Appendix A. Restricting our attention to small amplitude disturbances that arise from perturbing a resting basic state, we reach the following form of the governing equations,

$$
\begin{aligned}
\frac{\partial u}{\partial t} - \beta y v + \frac{\partial \phi}{\partial x} &= -\alpha u, \\
\frac{\partial v}{\partial t} + \beta y u + \frac{\partial \phi}{\partial y} &= -\alpha v, \\
\frac{\partial \phi}{\partial z} &= RT, \\
\frac{\partial u}{\partial x} + \frac{\partial v}{\partial y} + \frac{\partial w}{\partial z} - w &= 0, \\
\frac{\partial T}{\partial t} + \Gamma w &= -\alpha T + \frac{Q}{c_p},
\end{aligned}
\tag{2.6}
$$

where u is the eastward component of velocity, v the northward component, $w = Dz/Dt$ the "vertical log-pressure velocity," ϕ the perturbation geopotential, T the perturbation temperature, $\beta = 2\Omega/a$ the equatorial value of the northward gradient of the Coriolis parameter, Ω the Earth's rotation rate, a the Earth's radius, α the constant coefficient for Rayleigh friction and Newtonian cooling. We have assumed the frictional dissipation, F_x, F_y, takes the form, $-\alpha u$, $-\alpha v$, respectively. The total diabatic effect term, $\mathcal{D}$, has been partitioned into dissipation due to radiative cooling, $-\alpha T$, and generation due to convective heating, Q/c_p. The basic state static stability, $\Gamma = d\bar{T}/dz + \kappa\bar{T}$ ($\kappa = R/c_p$), is computed from the basic state temperature profile, $\bar{T}(z)$. For simplicity we assume that Γ is a constant, and choose the tropical tropospheric mean value $\Gamma = 23.79$ K. We seek solutions of (2.6) on a domain that is infinite in y, periodic over $-\pi a \le x \le \pi a$, and confined between $z = 0$ and $z = z_T = \ln(1010/200) \approx 1.619$, with the boundary conditions $w = 0$ at $z = 0, z_T$.

2.2   Separation of Horizontal and Vertical Structure

Our first step in solving the governing equations is to separate off the vertical structure. This is done by performing a vertical normal mode transform on equations (2.6). Appendix B details this process by following the treatment in Fulton and Schubert (1985), which results in the variables taking the following series forms,

$$
\begin{pmatrix} u(x,y,z,t) \\ v(x,y,z,t) \\ \phi(x,y,z,t) \end{pmatrix} = \sum_{\ell=1}^{\infty} \begin{pmatrix} u_\ell(x,y,t) \\ v_\ell(x,y,t) \\ \phi_\ell(x,y,t) \end{pmatrix} Z_\ell(z), \quad \begin{pmatrix} T(x,y,z,t) \\ w(x,y,z,t) \\ Q(x,y,z,t) \end{pmatrix} = \sum_{\ell=1}^{\infty} \begin{pmatrix} T_\ell(x,y,t) \\ w_\ell(x,y,t) \\ Q_\ell(x,y,t) \end{pmatrix} Z_\ell'(z),
$$

$$(2.7)$$

where the orthogonal functions $Z_\ell(z)$ and their derivatives $Z_\ell'(z) = (d/dz)Z_\ell(z)$ compose the vertical structure. The specific form of the vertical modes can be found by solving the Sturm-Liouville problem

$$
\left(\frac{d}{dz} - 1 \right) \frac{d}{dz} Z_\ell(z) = -\left(\frac{\ell^2 \pi^2}{z_T^2} + \frac{1}{4} \right) Z_\ell(z), \tag{2.8}
$$

$$
Z_\ell'(0) = Z_\ell'(z_T) = 0, \tag{2.9}
$$

which arose from imposed conditions during the separation process. The separation constants $\bar{c}_\ell^2$ turn out to be the square of the internal pure gravity wave phase speeds corresponding to the vertical internal modes $\ell = 1, 2, \ldots$ and are defined as

$$
\frac{R\Gamma}{\bar{c}_\ell^2} = \left(\frac{\ell^2 \pi^2}{z_T^2} + \frac{1}{4} \right)
$$

The first internal vertical mode $Z_1(z)$ and its derivative $Z_1'(z)$ can be written in normalized form as

$$
Z_1(z) = \left(\frac{\pi^2}{z_T^2} + \frac{1}{4} \right)^{-\frac{1}{2}} e^{(z-z_m)/2} \left[\frac{z_T}{2\pi} \sin\left(\frac{\pi z}{z_T} \right) - \cos\left(\frac{\pi z}{z_T} \right) \right], \tag{2.10}
$$

and

$$
Z_1'(z) = \left(1 + \frac{z_T^2}{4\pi^2} \right)^{\frac{1}{2}} e^{(z-z_m)/2} \sin\left(\frac{\pi z}{z_T} \right), \tag{2.11}
$$

where z_m, the level at which $Z_1'(z)$ reaches its maximum value, is given by $\pi z_m/z_T = \pi + \tan^{-1}(-2\pi/z_T)$, which, for $z_T \approx 1.619$, turns out to be $z_m \approx 0.5803 z_T$. For later
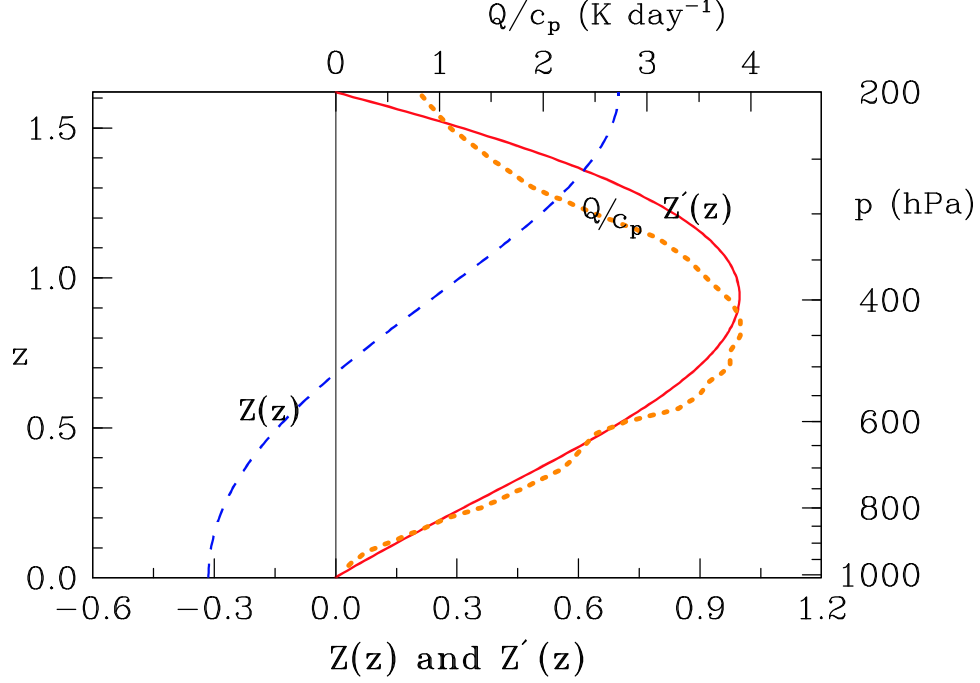
Figure 2.1: The curves labeled $Z(z)$ (blue,dashed) and $Z'(z)$ (red,solid)—interpreted using the lower scale—are the vertical structure functions defined by (2.10) and (2.11). The curve labeled Q/c_p (orange,dotted)—interpreted using the upper scale—is the 120-day mean vertical profile of heating rate for the western Pacific warm pool, as determined by Johnson and Ciesielski (2000). Note that $Z'(z)$ reaches its maximum at $p \approx 395$ hPa.

convenience, the normalization chosen in (2.10) and (2.11) yields $Z'_1(z_m) = 1$. Relabeling these functions to be $Z(z) \equiv Z_1(z)$ and $Z'(z) \equiv Z'_1(z)$, their plots are shown in Fig. 2.1. Also shown in Fig. 2.1 is the 120-day mean (November 1992 – February 1993) vertical profile of the heating rate for the western Pacific warm pool (Johnson and Ciesielski, 2000). The observed mean profile of Q/c_p has a peak value of approximately 4 K day^{-1}, and its shape is closely approximated by $Z'(z)$, the vertical structure of our constructed Q/c_p. Based on this good approximation we make the simplifying assumption that the heating excites only the first vertical internal mode. In doing so, the infinite series is truncated to this single mode. The variable expressions in (2.7) can then be rewritten as

$$\begin{pmatrix} u(x,y,z,t) \\ v(x,y,z,t) \\ \phi(x,y,z,t) \end{pmatrix} = \begin{pmatrix} \hat{u}(x,y,t) \\ \hat{v}(x,y,t) \\ \hat{\phi}(x,y,t) \end{pmatrix} Z(z), \qquad \begin{pmatrix} T(x,y,z,t) \\ w(x,y,z,t) \\ Q(x,y,z,t) \end{pmatrix} = \begin{pmatrix} \hat{T}(x,y,t) \\ \hat{w}(x,y,t) \\ \hat{Q}(x,y,t) \end{pmatrix} Z'(z), \qquad (2.12)$$

where the (^)'s on the transformed variables denote their lack of z-dependence. The gravity wave speed that corresponds to the first internal vertical mode is

$$\bar{c} \equiv \bar{c}_1 = \frac{(R\Gamma)^{1/2}}{\left[\frac{\pi^2}{z_T^2} + \frac{1}{4}\right]^{1/2}} \approx 41.25 \text{ m s}^{-1}. \tag{2.13}$$

Over the 120-day observational period there were two MJO passages (Lin and Johnson, 1996; Yanai et al., 2000). During these two periods of enhanced convection the shape of the vertical profile of Q/c_p was very similar to the shape of the time mean profile shown in Fig. 2.1, but the peak values were considerably larger, 10 K day^{-1} for the first MJO and 16 K day^{-1} for the second. Thus, for the vertical profile of heating at the time of peak convective activity during the passage of an MJO, our model uses the $Z'(z)$ profile shown in Fig. 2.1, but scaled so the peak value is 12 K day^{-1} (chosen as an intermediate value between the two MJO peak values) rather than 4 K day^{-1}. Assuming now that u, v, ϕ, T, w, Q have the separable forms given in (2.12) we can convert (2.6) into the following system for the horizontal structure functions $\hat{u}, \hat{v}, \hat{\phi}, \hat{T}, \hat{w}$:

$$
\begin{aligned}
\frac{\partial \hat{u}}{\partial t} - \beta y \hat{v} + \frac{\partial \hat{\phi}}{\partial x} &= -\alpha \hat{u}, \\
\frac{\partial \hat{v}}{\partial t} + \beta y \hat{u} + \frac{\partial \hat{\phi}}{\partial y} &= -\alpha \hat{v}, \\
\hat{\phi} &= R\hat{T}, \\
\frac{\partial \hat{u}}{\partial x} + \frac{\partial \hat{v}}{\partial y} - \left(\frac{\pi^2}{z_T^2} + \frac{1}{4}\right)\hat{w} &= 0, \\
\frac{\partial \hat{T}}{\partial t} + \Gamma \hat{w} &= -\alpha \hat{T} + \frac{\hat{Q}}{c_p}.
\end{aligned}
\tag{2.14}
$$

In section 2.4 we present an analytical solution of (2.14). The solution can be considered as the primitive equation generalization of the simplest MJO model involving the first baroclinic mode response to a moving planetary scale heat source under the long wave approximation (Chao, 1987).

2.3   Model Diabatic Forcing

A limitation of using prescribed forcing is that the flow field cannot exert any influence on it. In other words, the forcing acts on the model atmosphere altering its structure, though the circulation that results is not able to communicate its new state back to the forcing. If feedback from the circulation does not significantly change the "net effect" of the forcing, then this interaction could be neglected in a first approximation when large-scale features are of interest. Under this rationale we proceed forward with a prescribed diabatic forcing designed to resolve the net effect from an ensemble of convective cloud complexes (a general upward transport of mass). Thus, the multi-scale structure described in section 1.2 will not be captured, which is consistent with regard to scale when circulation feedbacks are not present.

$c_p = 1004$ J kg^{-1} K^{-1}	$\beta = 2\Omega/a$	$\bar{c} = 41.25$ m s^{-1}	$y_0 = 0$ or 450 km
$R = 287$ J kg^{-1} K^{-1}	$p_0 = 1010$ hPa	$\epsilon = 507.3$	$Q_0/c_p = 12$ K day^{-1}
$\Omega = 7.292 \times 10^{-5}$ s^{-1}	$z_T = 1.619$	$a_0 = 1250$ km	$c = 5$ m s^{-1}
$a = 6370$ km	$\Gamma = 23.79$ K	$b_0 = 450$ km	$\alpha = (4 \text{ days})^{-1}$

Table 2.1: Constants.

Since the diabatic forcing is due to an eastward propagating region of deep convection, a suitable zonal structure is a sinusoid function of $x - ct$, where $c > 0$ is the constant propagation speed of the cloud cluster. The exact form of the horizontal structure is given by

$$\hat{Q}(x,y,t) = \tfrac{1}{2}Q_0 \exp\left[-\left(\tfrac{y-y_0}{b_0}\right)^2\right] \begin{cases} 1 + \cos\left(\pi\xi/a_0\right) & |\xi| \leq a_0, \\ \\ 0 & |\xi| \geq a_0, \end{cases} \qquad (2.15)$$

$\xi = x - ct$, y_0 its center, a_0 its half-width in x, b_0 its e-folding width in y, and Q_0 its peak amplitude. The values chosen for these parameters are listed in Table 2.1. The choices for a_0, b_0, and y_0 were based on reanalysis studies discussed in section 1.2, the value for Q_0 was based on observations during TOGA-COARE, discussed in section 2.2. A plot of (2.15) with $Q_0 = 1$ J kg^{-1}s^{-1} is shown in Fig. 2.2. It is interesting to note that the area integral
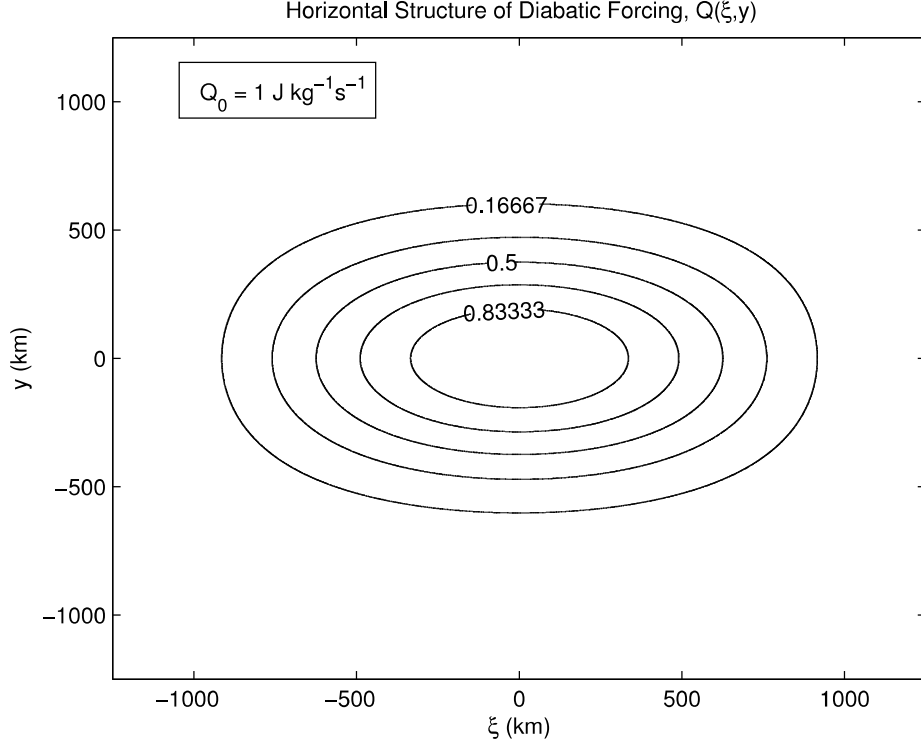
Figure 2.2: Contour plot of the diabatic forcing horizontal structure with Q_0 set to 1 J kg^{-1}s^{-1}.

of (2.15) yields $\iint \hat{Q}(\xi, y)\, dx dy = \pi^{\frac{1}{2}} Q_0 a_0 b_0$, so that our variation of the parameter y_0 has no effect on the total diabatic heating rate, $\pi^{\frac{1}{2}} Q_0 a_0 b_0$.

2.4   Horizontal Structure Problem

Our interest is in observing the flow field around the eastward moving constant source once all transient effects have ended. If we assume that it does reach a steady state, then viewing it from a reference frame that is moving at the same speed as the source would allow us to study the unchanging response pattern, versus watching the evolution of a particular region as the source passes through it. From this vantage point a change in time is proportional to a change in zonal position of the earth-relative steady state circulation. The shallow water equations (2.14) are converted to a system that is valid in this moving frame of reference by transforming both time and zonal derivatives to derivatives of the

"translating zonal distance coordinate" (ξ), introduced in the previous section. Making the replacements (see Appendix C for justification)

$$\frac{\partial}{\partial x} = \frac{\partial}{\partial \xi}, \tag{2.16}$$

$$\frac{\partial}{\partial t} = -c\frac{\partial}{\partial \xi}, \tag{2.17}$$

in (2.14) results in

$$
\begin{aligned}
-c\frac{\partial \hat{u}}{\partial \xi} - \beta y \hat{v} + \frac{\partial \hat{\phi}}{\partial \xi} &= -\alpha \hat{u}, \\
-c\frac{\partial \hat{v}}{\partial \xi} + \beta y \hat{u} + \frac{\partial \hat{\phi}}{\partial y} &= -\alpha \hat{v}, \\
\hat{\phi} &= R\hat{T}, \\
\frac{\partial \hat{u}}{\partial \xi} + \frac{\partial \hat{v}}{\partial y} - \left(\frac{\pi^2}{z_T^2} + \frac{1}{4}\right)\hat{w} &= 0, \\
-c\frac{\partial \hat{T}}{\partial \xi} + \Gamma \hat{w} &= -\alpha \hat{T} + \frac{\hat{Q}}{c_p},
\end{aligned}
\tag{2.18}
$$

reducing the number of independent variables from three to two. Next take the Fourier ξ-transform of the resulting system, defining, for example,

$$\hat{u}_m(y) = \frac{1}{2\pi a}\int_{-\pi a}^{\pi a}\hat{u}(\xi, y)e^{-im\xi/a}d\xi, \quad \hat{u}(\xi, y) = \sum_{m=-\infty}^{\infty}\hat{u}_m(y)e^{im\xi/a}, \tag{2.19}$$

where the integer m denotes the zonal wavenumber. Similar Fourier transform pairs exist for $\hat{v}_m(y)$, $\hat{\phi}_m(y)$, $\hat{T}_m(y)$, $\hat{w}_m(y)$, and $\hat{Q}_m(y)$. In this way, system (2.18) reduces to

$$
\begin{aligned}
\left(\alpha - \frac{imc}{a}\right)\hat{u}_m - \beta y \hat{v}_m + \frac{im}{a}\hat{\phi}_m &= 0, \\
\left(\alpha - \frac{imc}{a}\right)\hat{v}_m + \beta y \hat{u}_m + \frac{d\hat{\phi}_m}{dy} &= 0, \\
\left(\alpha - \frac{imc}{a}\right)\hat{\phi}_m + \bar{c}^2\left(\frac{im}{a}\hat{u}_m + \frac{d\hat{v}_m}{dy}\right) &= \kappa \hat{Q}_m,
\end{aligned}
\tag{2.20}
$$

after eliminating $\hat{w}_m$ and $\hat{T}_m$ by combining the hydrostatic, continuity, and thermodynamic equations. For each integer wavenumber m, (2.20) is a system of equations dependent only on meridional position. Once (2.20) has been solved for $\hat{u}_m$, $\hat{v}_m$, $\hat{\phi}_m$, the vertical velocity $\hat{w}_m$ can be recovered from

$$\hat{w}_m = \left(\frac{\pi^2}{z_T^2} + \frac{1}{4}\right)^{-1}\left(\frac{im}{a}\hat{u}_m + \frac{d\hat{v}_m}{dy}\right). \tag{2.21}$$

The Fourier ξ-transform of $\hat{Q}(\xi, y)$, defined by (2.15), is given by

$$\hat{Q}_m(y) = (2\pi a)^{-1} \int_{-\pi a}^{\pi a} \hat{Q}(\xi, y) \exp(-im\xi/a)d\xi,$$

which is easily evaluated to yield

$$\hat{Q}_m(y) = \frac{\pi Q_0}{2[\pi^2 - (ma_0/a)^2]} \frac{\sin(ma_0/a)}{m} \exp\left[-\left(\frac{y - y_0}{b_0} \right)^2 \right]. \tag{2.22}$$

We now write the system (2.20) in the convenient vector form [1]

$$\left(\alpha - \frac{imc}{a} \right) \hat{\boldsymbol{\eta}}_m + \mathcal{L}\hat{\boldsymbol{\eta}}_m = \kappa \hat{\mathbf{Q}}_m, \tag{2.23}$$

where

$$\mathcal{L} = \begin{pmatrix} 0 & -\beta y & im/a \\ \beta y & 0 & d/dy \\ \bar{c}^2 im/a & \bar{c}^2 d/dy & 0 \end{pmatrix}, \quad \hat{\boldsymbol{\eta}}_m(y) = \begin{pmatrix} \hat{u}_m(y) \\ \hat{v}_m(y) \\ \hat{\phi}_m(y) \end{pmatrix}, \quad \hat{\mathbf{Q}}_m(y) = \begin{pmatrix} 0 \\ 0 \\ \hat{Q}_m(y) \end{pmatrix}. \tag{2.24}$$

The Fourier transformed equations (2.23) can be solved using a normal mode transform in the meridional direction. To accomplish this, first define the inner product

$$(\mathbf{f}, \mathbf{g}) = \int_{-\infty}^{\infty} \left(f_1 g_1^* + f_2 g_2^* + \frac{1}{\bar{c}^2} f_3 g_3^* \right) d\hat{y}, \tag{2.25}$$

where $\mathbf{f}(\hat{y})$ and $\mathbf{g}(\hat{y})$ are complex, three component vector functions of the dimensionless meridional coordinate $\hat{y} = (\beta/\bar{c})^{\frac{1}{2}} y = \epsilon^{\frac{1}{4}}(y/a)$, and where the * symbol denotes the complex conjugate and $\epsilon = 4\Omega^2 a^2/\bar{c}^2$ is Lamb's parameter. With $\bar{c} = 41.25$ m s^{-1} we obtain $\epsilon = 507.3$. The inner product (2.25), is suggested by the total energy principle (derived in section 4.1) associated with (2.23). The adjoint of $\mathcal{L}$, denoted by $\mathcal{L}^\dagger$ and defined by $(\mathcal{L}\mathbf{f}, \mathbf{g}) = (\mathbf{f}, \mathcal{L}^\dagger \mathbf{g})$, is related to $\mathcal{L}$ by $\mathcal{L}^\dagger = -\mathcal{L}$. In other words, the linear operator $\mathcal{L}$ is skew-Hermitian with respect to the inner product (2.25). The skew-Hermitian property dictates that the eigenvalues of $\mathcal{L}$ are pure imaginary and that the eigenfunctions form a complete

---

[1] The simplicity of the first term in (2.23) depends on the assumed equality for the damping rates associated with Rayleigh friction and Newtonian cooling. However, the derivation following (2.23) could easily be generalized to allow a 10–20 day radiative damping rate and a 3–5 day frictional damping rate (Lin et al., 2005).

(Wu and Moore, 2004), orthogonal set (as long as degeneracy does not occur). Denoting an eigenvalue by $i\nu_{mnr}$ and a corresponding eigenfunction by $\mathbf{K}_{mnr}(\hat{y})$, we have

$$\mathcal{L}\mathbf{K}_{mnr} = i\nu_{mnr}\mathbf{K}_{mnr}, \quad \text{with} \quad \mathbf{K}_{mnr}(\hat{y}) = \begin{pmatrix} U_{mnr}(\hat{y}) \\ V_{mnr}(\hat{y}) \\ \Phi_{mnr}(\hat{y}) \end{pmatrix}. \tag{2.26}$$

The eigenvalues of $\mathcal{L}$, which yield the dispersion relation for equatorially trapped waves,
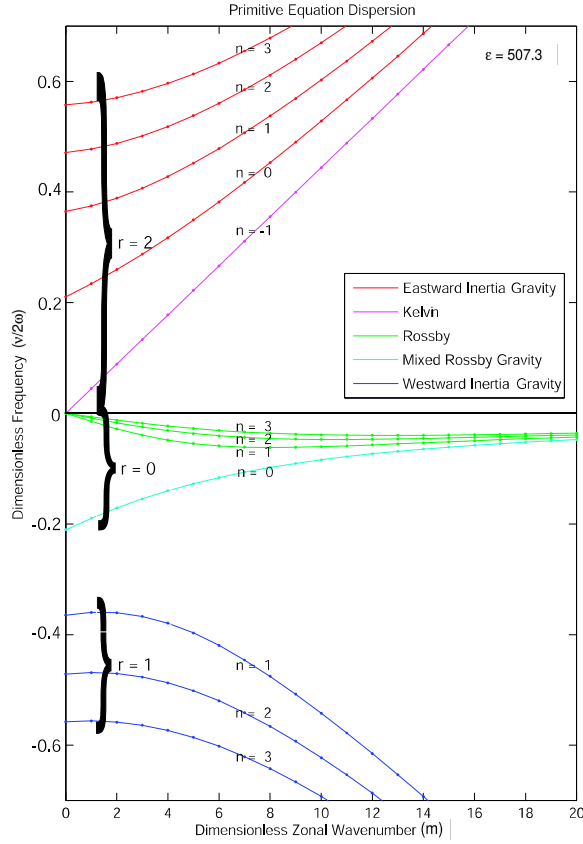

Figure 2.3: Dispersion diagram, $\hat{\nu}_{mnr}$ vs. m, for values $n = -1, 0, 1, 2, 3$ and $r = 0, 1, 2$.

satisfy the cubic equation (Matsuno, 1966)

$$\epsilon\hat{\nu}^2 - m^2 - \frac{m}{\hat{\nu}} = \epsilon^{\frac{1}{2}}(2n+1), \tag{2.27}$$

where $n = 0, 1, 2, \cdots$ is the index for the meridional mode and $\hat{\nu} = \nu/(2\Omega)$ is the dimensionless frequency. We let $r = 0, 1, 2$ be the index corresponding to the three roots of the

dispersion relation, so that the eigenfunctions and eigenvalues can be characterized by the triple index m, n, r. Special care is required for the case $n = 0$, for which (2.27) can be factored into $(\epsilon^{\frac{1}{2}}\hat{\nu} + m)(\epsilon^{\frac{1}{2}}\hat{\nu}^2 - m\hat{\nu} - 1) = 0$. The root $\epsilon^{\frac{1}{2}}\hat{\nu} = -m$ must be discarded because the corresponding eigenfunction is unbounded in $\hat{y}$. Thus, when $n = 0$, only the two solutions of $\epsilon^{\frac{1}{2}}\hat{\nu}^2 - m\hat{\nu} - 1 = 0$ are retained and are indexed by $r = 0$ (mixed Rossby-gravity wave) and $r = 2$ (eastward inertia-gravity wave). The eigenfunctions for Kelvin waves can be found separately by setting V_{mnr} to zero in (2.26). The Kelvin wave eigenvalues $\epsilon^{\frac{1}{2}}\hat{\nu} = m$ can be formally considered as a solution to (2.27) when $n = -1$. We index this solution as $r = 2$. Then, for given $n = -1, 0, 1, \cdots$, $\mathbf{K}_{mnr}(\hat{y})$ is the eigenfunction corresponding to the eigenvalue ν_{mnr}. The form of $\mathbf{K}_{mnr}(\hat{y})$ is given by

$$\mathbf{K}_{mnr}(\hat{y}) = A_{mnr} \begin{pmatrix} \epsilon^{\frac{1}{4}} \left[\left(\epsilon^{\frac{1}{2}}\hat{\nu}_{mnr} + m \right) \left(\frac{n+1}{2} \right)^{\frac{1}{2}} \mathcal{H}_{n+1}(\hat{y}) + \left(\epsilon^{\frac{1}{2}}\hat{\nu}_{mnr} - m \right) \left(\frac{n}{2} \right)^{\frac{1}{2}} \mathcal{H}_{n-1}(\hat{y}) \right] \\ -i \left(\epsilon\hat{\nu}_{mnr}^2 - m^2 \right) \mathcal{H}_n(\hat{y}) \\ \bar{c}\epsilon^{\frac{1}{4}} \left[\left(\epsilon^{\frac{1}{2}}\hat{\nu}_{mnr} + m \right) \left(\frac{n+1}{2} \right)^{\frac{1}{2}} \mathcal{H}_{n+1}(\hat{y}) - \left(\epsilon^{\frac{1}{2}}\hat{\nu}_{mnr} - m \right) \left(\frac{n}{2} \right)^{\frac{1}{2}} \mathcal{H}_{n-1}(\hat{y}) \right] \end{pmatrix},$$

(2.28)

where the meridional structure functions $\mathcal{H}_n(\hat{y})$ $(n = 0, 1, 2, \ldots)$ are related to the Hermite polynomials $H_n(\hat{y})$ $(n = 0, 1, 2, \ldots)$ by [2]

$$\mathcal{H}_n(\hat{y}) = \left(\pi^{\frac{1}{2}} 2^n n! \right)^{-\frac{1}{2}} H_n(\hat{y}) e^{-\frac{1}{2}\hat{y}^2}. \tag{2.29}$$

Since the Hermite polynomials satisfy the recurrence relation $\hat{y}H_n(\hat{y}) = \frac{1}{2}H_{n+1}(\hat{y}) + nH_{n-1}(\hat{y})$ and the derivative relation $dH_n(\hat{y})/d\hat{y} = 2nH_{n-1}(\hat{y})$, it is easily shown that the meridional structure functions $\mathcal{H}_n(\hat{y})$ satisfy the recurrence relation

$$\hat{y}\mathcal{H}_n(\hat{y}) = \left(\frac{n+1}{2} \right)^{\frac{1}{2}} \mathcal{H}_{n+1}(\hat{y}) + \left(\frac{n}{2} \right)^{\frac{1}{2}} \mathcal{H}_{n-1}(\hat{y}), \tag{2.30}$$

and the derivative relation

$$\frac{d\mathcal{H}_n(\hat{y})}{d\hat{y}} = -\left(\frac{n+1}{2} \right)^{\frac{1}{2}} \mathcal{H}_{n+1}(\hat{y}) + \left(\frac{n}{2} \right)^{\frac{1}{2}} \mathcal{H}_{n-1}(\hat{y}). \tag{2.31}$$

---

[2] The meridional structure functions $\mathcal{H}_n$ are more convenient for our purposes than the parabolic cylinder functions D_n. The two functions are related by $\mathcal{H}_n(\hat{y}) = (\pi^{\frac{1}{2}}n!)^{-\frac{1}{2}} D_n(2^{\frac{1}{2}}\hat{y})$.
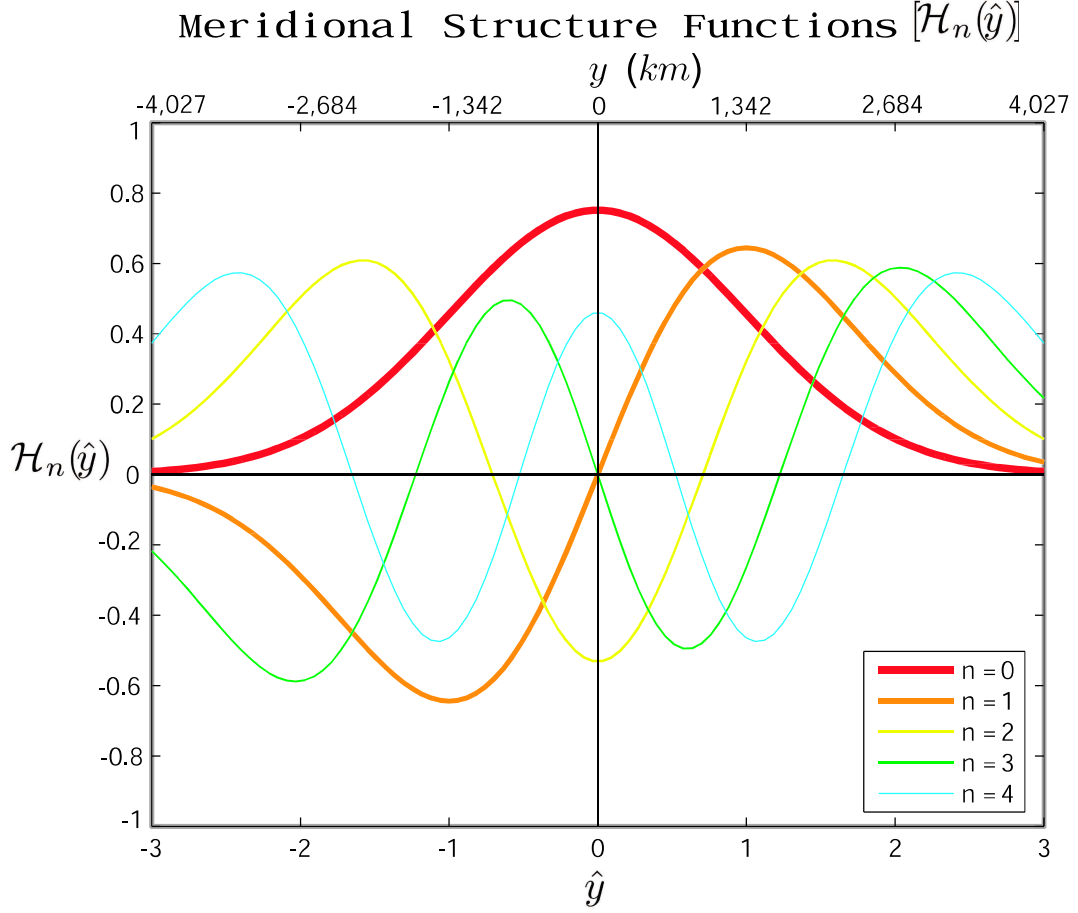
Figure 2.4: The meridional structure functions, $\mathcal{H}_n(\hat{y})$ for $n = 0, 1, 2, 3, 4$, are plotted over the equatorial band $\sim (35°\text{S}, 35°\text{N})$. The lower axis displays dimensionless meridional distance, $\hat{y} = \epsilon^{\frac{1}{4}}(y/a)$, and the upper axis displays the corresponding (integer) dimensional meridional distance, y km.

The first two meridional structure functions are $\mathcal{H}_0(\hat{y}) = \pi^{-\frac{1}{4}}e^{-\frac{1}{2}\hat{y}^2}$ and $\mathcal{H}_1(\hat{y}) = 2^{\frac{1}{2}}\pi^{-\frac{1}{4}}\hat{y}e^{-\frac{1}{2}\hat{y}^2}$, from which all succeeding structure functions can be computed using the recurrence relation (2.30). Computing $\mathcal{H}_n(\hat{y})$ via its recurrence relation is much preferable to computing $H_n(\hat{y})$ via its recurrence relation and then computing $\mathcal{H}_n(\hat{y})$ by evaluation of the right hand side of (2.29), because the former method avoids explicit calculation of the factor $2^n n!$ for large n. Plots of $\mathcal{H}_n(\hat{y})$ for $n = 0, 1, 2, 3, 4$ are shown in Fig. 2.4. The normalization factor in (2.28) is given by

$$A_{mnr} = \left[\epsilon^{\frac{1}{2}}(n+1)\left(\epsilon^{\frac{1}{2}}\hat{\nu}_{mnr} + m\right)^2 + \epsilon^{\frac{1}{2}}n\left(\epsilon^{\frac{1}{2}}\hat{\nu}_{mnr} - m\right)^2 + \left(\epsilon\hat{\nu}_{mnr}^2 - m^2\right)^2\right]^{-\frac{1}{2}} \quad (2.32)$$

for $n \geq 0$ and by

$$A_{m,-1,2} = 2^{-\frac{1}{2}} \pi^{-\frac{1}{4}} \tag{2.33}$$

for $n = -1$. These normalization factors result in the orthonormality property

$$\left(\mathbf{K}_{mnr}(\hat{y}), \mathbf{K}_{mn'r'}(\hat{y}) \right) = \begin{cases} 1 & (n', r') = (n, r) \\ 0 & (n', r') \neq (n, r). \end{cases} \tag{2.34}$$

The normality part of (2.34) is easily confirmed by substituting (2.28) into the left hand side and then using

$$\int_{-\infty}^{\infty} \mathcal{H}_n(\hat{y}) \mathcal{H}_{n'}(\hat{y}) d\hat{y} = \begin{cases} 1 & n' = n, \\ 0 & n' \neq n \end{cases} \tag{2.35}$$

to evaluate the three resulting integrals. It should be noted that there is a degeneracy for the zonally symmetric Rossby modes (i.e., for $m = 0$, $n > 0$, $r = 0$), in which case (2.28) is indeterminant because both m and $\hat{\nu}_{0n0}$ vanish. However, orthonormal eigenfunctions are easily constructed in this case, as discussed in Appendix D. Because of the orthonormality and completeness of the eigenfunctions $\mathbf{K}_{mnr}(\hat{y})$, we can set up the transform pair (Silva Dias et al., 1983; DeMaria, 1985)

$$\hat{\eta}_{mnr} = \left(\hat{\boldsymbol{\eta}}_m(\hat{y}), \mathbf{K}_{mnr}(\hat{y}) \right), \tag{2.36}$$

$$\hat{\boldsymbol{\eta}}_m(\hat{y}) = \sum_{n=-1}^{\infty} \sum_r \hat{\eta}_{mnr} \mathbf{K}_{mnr}(\hat{y}), \tag{2.37}$$

where $\hat{\eta}_{mnr}$ are the scalar coefficients in the normal mode expansion of the vector $\hat{\boldsymbol{\eta}}_m(\hat{y})$. Note that (2.36) can be obtained by taking the inner product of (2.37) with $\mathbf{K}_{mn'r'}(\hat{y})$ and using the orthonormality property (2.34).

We now have the tools necessary to solve (2.23). Start by taking the inner product of (2.23) with the eigenfunction $\mathbf{K}_{mnr}(\hat{y})$,

$$\left(\left(\alpha - \frac{imc}{a} \right) \hat{\boldsymbol{\eta}}_m, \mathbf{K}_{mnr}(\hat{y}) \right) + (\mathcal{L}\hat{\boldsymbol{\eta}}_m, \mathbf{K}_{mnr}(\hat{y})) = \left(\kappa \hat{\mathbf{Q}}_m, \mathbf{K}_{mnr}(\hat{y}) \right),$$

next use the Skew-Hermitian property of $\mathcal{L}$,

$$\left(\alpha - \frac{imc}{a} \right) (\hat{\boldsymbol{\eta}}_m, \mathbf{K}_{mnr}(\hat{y})) + (\hat{\boldsymbol{\eta}}_m, -\mathcal{L}\mathbf{K}_{mnr}(\hat{y})) = \kappa \left(\hat{\mathbf{Q}}_m, \mathbf{K}_{mnr}(\hat{y}) \right),$$

use the eigen-relation (2.26), (2.36), and the inner product $\hat{Q}_{mnr} = (\hat{\mathbf{Q}}_m, \mathbf{K}_{mnr})$,

$$\left(\alpha - \frac{imc}{a}\right)\hat{\eta}_{mnr} + i\nu_{mnr}\left(\hat{\boldsymbol{\eta}}_m, \mathbf{K}_{mnr}(\hat{y})\right) = \kappa\hat{Q}_{mnr},$$

finally,

$$\hat{\eta}_{mnr} = \frac{\kappa\hat{Q}_{mnr}}{\alpha + i(\nu_{mnr} - cm/a)}. \tag{2.38}$$

We have reduced the set of ordinary differential equations (2.23), to a decoupled system of algebraic equations (2.38), which can be solved independently for the values of $\hat{\eta}_{mnr}$. An expression for $(\hat{\mathbf{Q}}_m, \mathbf{K}_{mnr})$ is derived using the integral given in Appendix E. Using the result (E.1) twice, once with n replaced by $n+1$ and once with n replaced by $n-1$, we can write $\hat{Q}_{mnr}$ as

$$\begin{aligned}
\hat{Q}_{mnr} =& \frac{A_{mnr}\epsilon^{\frac{1}{2}}\pi Q_0 a_0 b_0}{2\bar{c}a^2[\pi^2 - (ma_0/a)^2]}\frac{\sin(ma_0/a)}{(ma_0/a)}\left(\frac{2\pi}{2+\hat{b}_0^2}\right)^{\frac{1}{2}}\exp\left(\frac{\hat{b}_0^2\hat{y}_0^2}{4-\hat{b}_0^4}\right)\\
&\cdot\left[(\epsilon^{\frac{1}{2}}\hat{\nu}_{mnr} + m)\left(\frac{2-\hat{b}_0^2}{2+\hat{b}_0^2}\right)^{\frac{n+1}{2}}\left(\frac{n+1}{2}\right)^{\frac{1}{2}}\mathcal{H}_{n+1}\left(\frac{2\hat{y}_0}{(4-\hat{b}_0^4)^{\frac{1}{2}}}\right)\right.\\
&\left.- (\epsilon^{\frac{1}{2}}\hat{\nu}_{mnr} - m)\left(\frac{2-\hat{b}_0^2}{2+\hat{b}_0^2}\right)^{\frac{n-1}{2}}\left(\frac{n}{2}\right)^{\frac{1}{2}}\mathcal{H}_{n-1}\left(\frac{2\hat{y}_0}{(4-\hat{b}_0^4)^{\frac{1}{2}}}\right)\right]
\end{aligned} \tag{2.39}$$

for $n \geq 0$, and as

$$\hat{Q}_{mnr} = \frac{A_{mnr}\epsilon^{\frac{1}{4}}\pi Q_0 a_0 b_0}{2\bar{c}a^2[\pi^2 - (ma_0/a)^2]}\frac{\sin(ma_0/a)}{(ma_0/a)}\left(\frac{2\pi}{2+\hat{b}_0^2}\right)^{\frac{1}{2}}\exp\left(-\frac{\hat{y}_0^2}{2+\hat{b}_0^2}\right). \tag{2.40}$$

for the Kelvin wave ($n = -1$, $r = 2$).

After $\hat{\eta}_{mnr}$ is computed from (2.38)–(2.40), the physical space fields u, v, ϕ can be recovered by making use of (2.37), followed by the inverse Fourier transform in ξ, i.e.,

$$\begin{pmatrix} u(\xi,y,z) \\ v(\xi,y,z) \\ \phi(\xi,y,z) \end{pmatrix} = Z(z)\sum_{m=-\infty}^{\infty}\sum_{n=-1}^{\infty}\sum_r \hat{\eta}_{mnr}\begin{pmatrix} U_{mnr}(\hat{y}) \\ V_{mnr}(\hat{y}) \\ \Phi_{mnr}(\hat{y}) \end{pmatrix}e^{im\xi/a}. \tag{2.41}$$

Using (2.21), (2.28) and (2.31) the physical space vertical log-pressure velocity can be recovered from

$$w(\xi,y,z) = \frac{Z'(z)}{R\Gamma}\sum_{m=-\infty}^{\infty}\sum_{n=-1}^{\infty}\sum_r i\nu_{mnr}\hat{\eta}_{mnr}\Phi_{mnr}(\hat{y})e^{im\xi/a}. \tag{2.42}$$

For later use we note that the vertical log-pressure velocity $w = Dz/Dt$ is related to the vertical p-velocity $\omega = Dp/Dt$ by $\omega = -p_0 e^{-z} w$.

2.5   Solutions

All the model results shown in this section have been constructed by numerical evaluation of (2.41), and (2.42), which involves a superposition of zonal wavenumbers (sum over m), meridional wavenumbers (sum over n), and wave types (sum over r). In our examples the spectral coefficients $\hat{\eta}_{mnr}$ decay exponentially with n for all choices of m, which enables us to truncate the spectral solution at $n = N$ with a specified degree of accuracy. In general, $N = 200$ gives accurate results. Appendix F displays a flow chart outlining the procedure for computing the solutions.

Although the solutions have been computed over the entire zonal domain, only half the domain, centered on the forcing, is shown. This allows greater detail to be displayed for the region nearest the forcing. Using the parameters listed in Table 2.1, the 850 hPa wind and geopotential fields computed from (2.41) are shown in the top panel of Fig. 2.5 for $y_0 = 0$ and in the top panel of Fig. 2.7 for $y_0 = 450$ km. The choice of 850 hPa as the display level is arbitrary. According to the profile of $Z(z)$ shown in Fig. 2.1, upper tropospheric fields have the opposite sign and approximately twice the magnitude of the lower tropospheric fields. An interesting property of these simple linear solutions is that the lower tropospheric maximum westerly winds in the wake of the convective envelope are stronger than the lower tropospheric maximum easterly winds ahead of the convection. For example, in Fig. 2.5 the maximum 850 hPa westerly flow is 3.7 m s^{-1} while the maximum easterly flow is 1.6 m s^{-1}. In Fig. 2.7 the corresponding values are 4.2 m s^{-1} and 1.4 m s^{-1}. These wind speeds, the degree of asymmetry between westerlies and easterlies, and the larger zonal extent of the easterlies compared to the westerlies all agree well with the observed MJO composite [3]

---

[3] There is substantial variability in the cases that make up the MJO composite so that a detailed comparison of model results with an individual MJO case probably requires modeling the details of the diabatic forcing associated with that case.

(see Figs. 1.4 and 1.5) presented by Kiladis et al. (2005, Figs. 2 and 3). The remaining panels of Figs. 2.5 show the decomposition of the total fields into Rossby modes ($r = 0$ with $n \geq 1$), inertia-gravity modes ($r = 1, 2$ with $n \geq 1$ and $r = 2$ with $n = 0$), and Kelvin modes ($r = 2$ with $n = -1$). We have not plotted the contribution from mixed Rossby-gravity modes ($r = 0$ with $n = 0$) since it vanishes when $y_0 = 0$. The remaining panels in Fig. 2.7 show the same components as in Fig. 2.5, but also present is the mixed Rossby-gravity mode because it is nonzero when $y_0 \neq 0$. It should be noted that for small displacements off the equator the mixed Rossby-gravity response is negligible compared with the other components and was shown here only for completeness. The 395 hPa vertical motion field (recall that $Z'(z)$ reaches its maximum amplitude at $p \approx 395$ hPa) computed from (2.42) is shown in the top panel of Fig. 2.6 for $y_0 = 0$ and in the top panel of Fig. 2.8 for $y_0 = 450$ km. The other panels of Figs. 2.6 and 2.8 show the same components for the vertical motion field as were shown of the circulation in Figs. 2.5 and 2.7, respectively. These figures show that the vertical motion field is primarily composed of the Kelvin and inertia-gravity response as the Rossby vertical motion is very small for any value of y_0, and the mixed-Rossby gravity response is identically zero on the equator, and relatively small otherwise.

Some notable features are apparent from Figs. 2.5–2.8. The total u, v, ϕ fields are composed of Rossby waves on the west side of the source, Kelvin waves on the east side, with "slaved" inertia-gravity waves providing low-level convergence near the source. As the center of the convective envelope is shifted north of the equator there is very little change in the response east of the forcing. In contrast, the response west of the forcing becomes biased to the northern hemisphere.
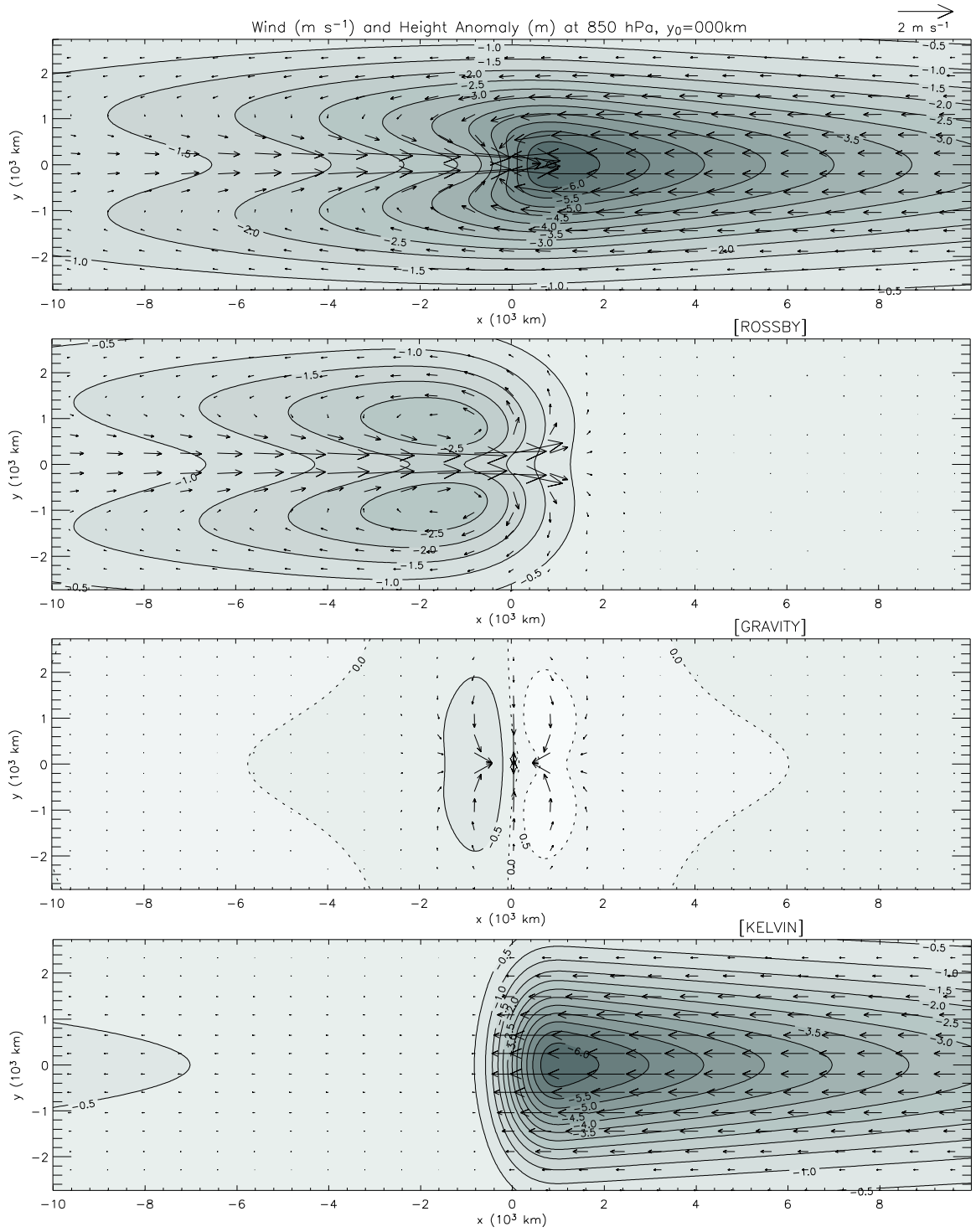
Figure 2.5: The upper panel shows the geopotential height anomaly and winds at 850 hPa for $y_0 = 0$ and for the remaining parameters listed in Table 2.1. The remaining three panels show respectively the contributions made by Rossby waves, inertia-gravity waves, and Kelvin waves.
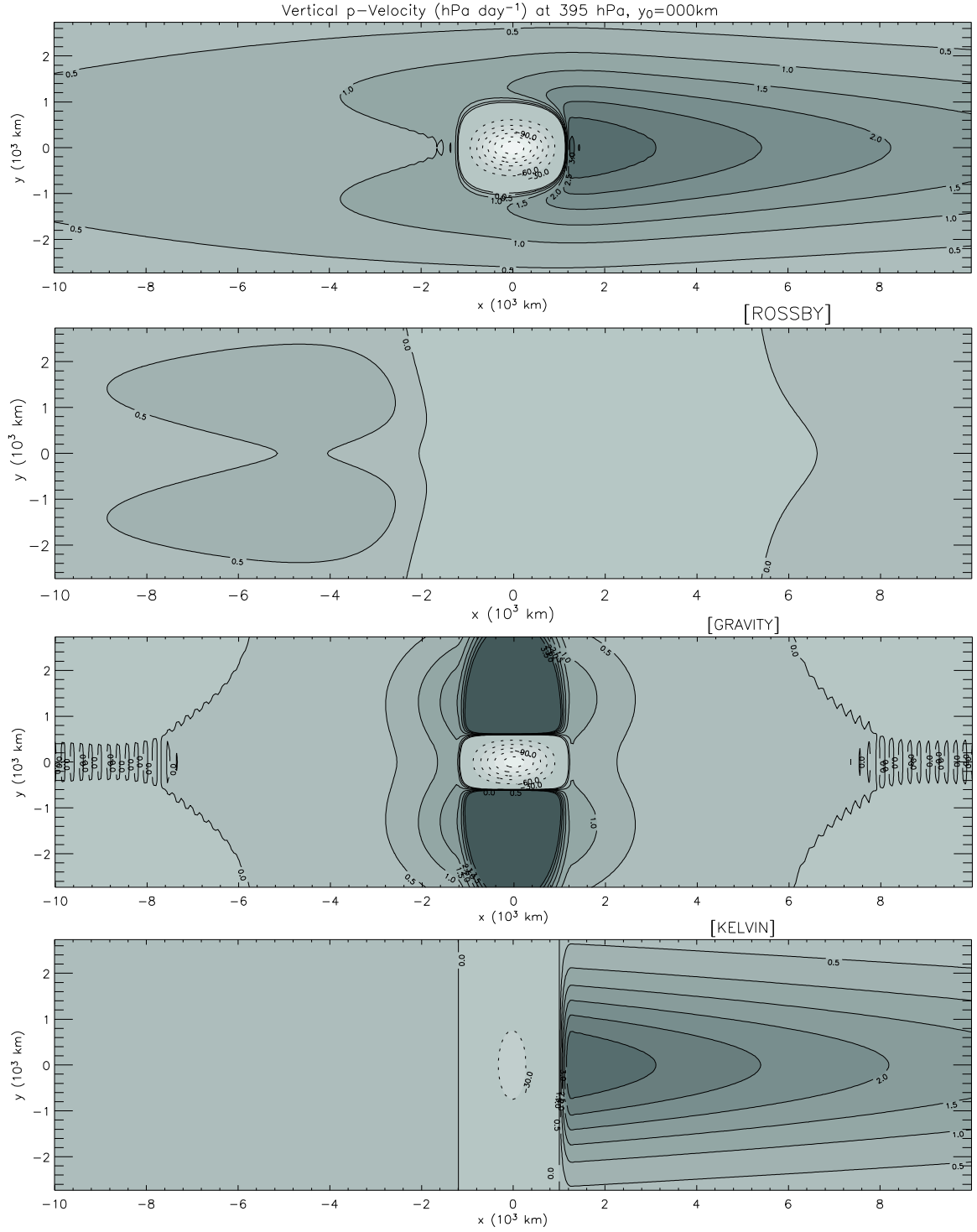
Figure 2.6: The first panel shows the vertical *p*-velocity, ω, at 395 hPa, with a contour interval of 30 hPa day^{-1} in the region of rising motion (dashed contours), and a contour interval of 0.5 hPa day^{-1} in the region of sinking motion (solid contours). The remaining panels show respective contributions of Rossby waves, inertia-gravity waves, and Kelvin waves to the vertical motion field. Results in this figure are for $y_0 = 0$.
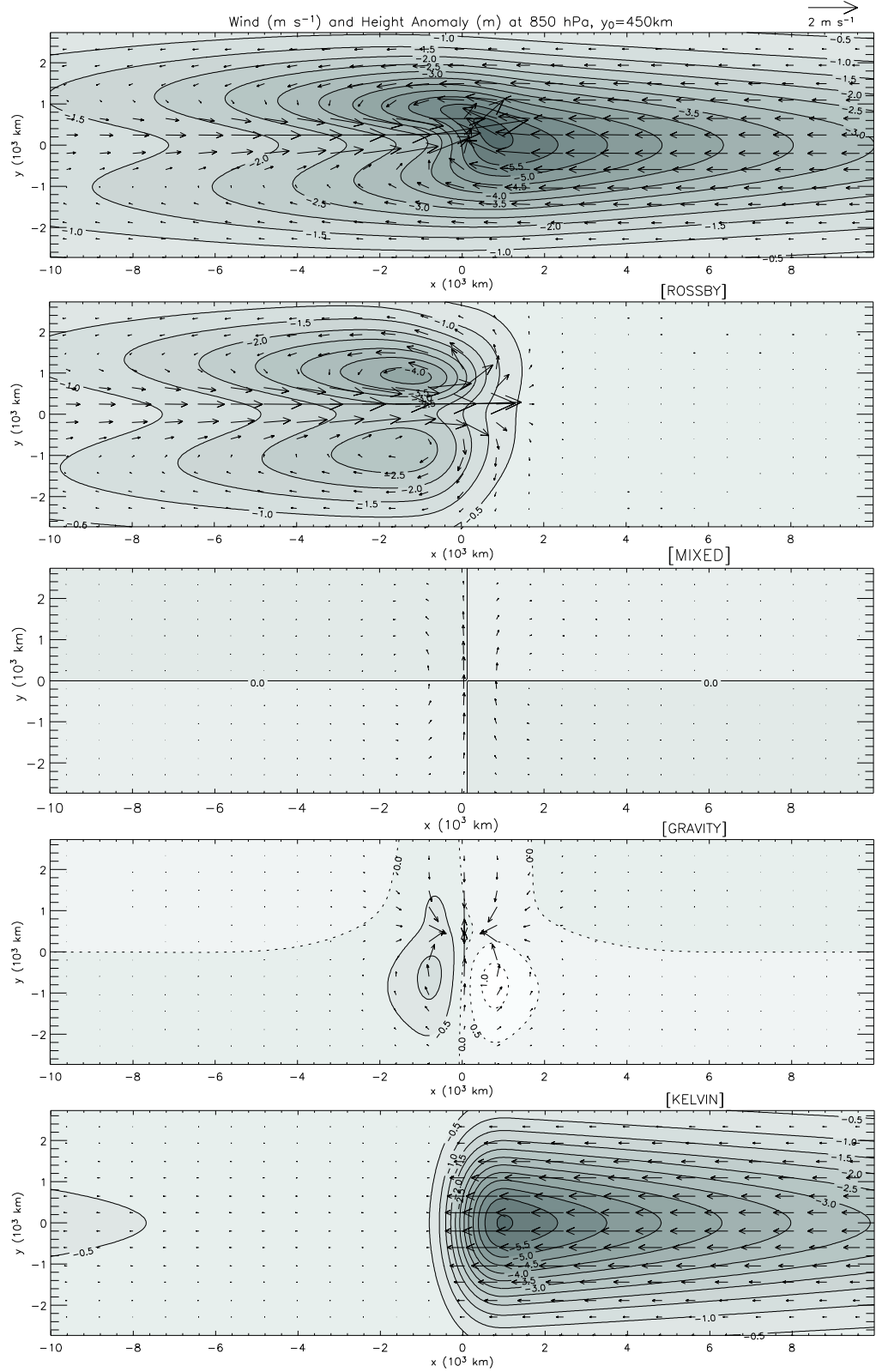
Figure 2.7: Same as Fig. 2.5, but the center of the convective forcing is shifted north of the equator ($y_0 = 450$ km), so the nonzero mixed Rossby-gravity component is shown as well.
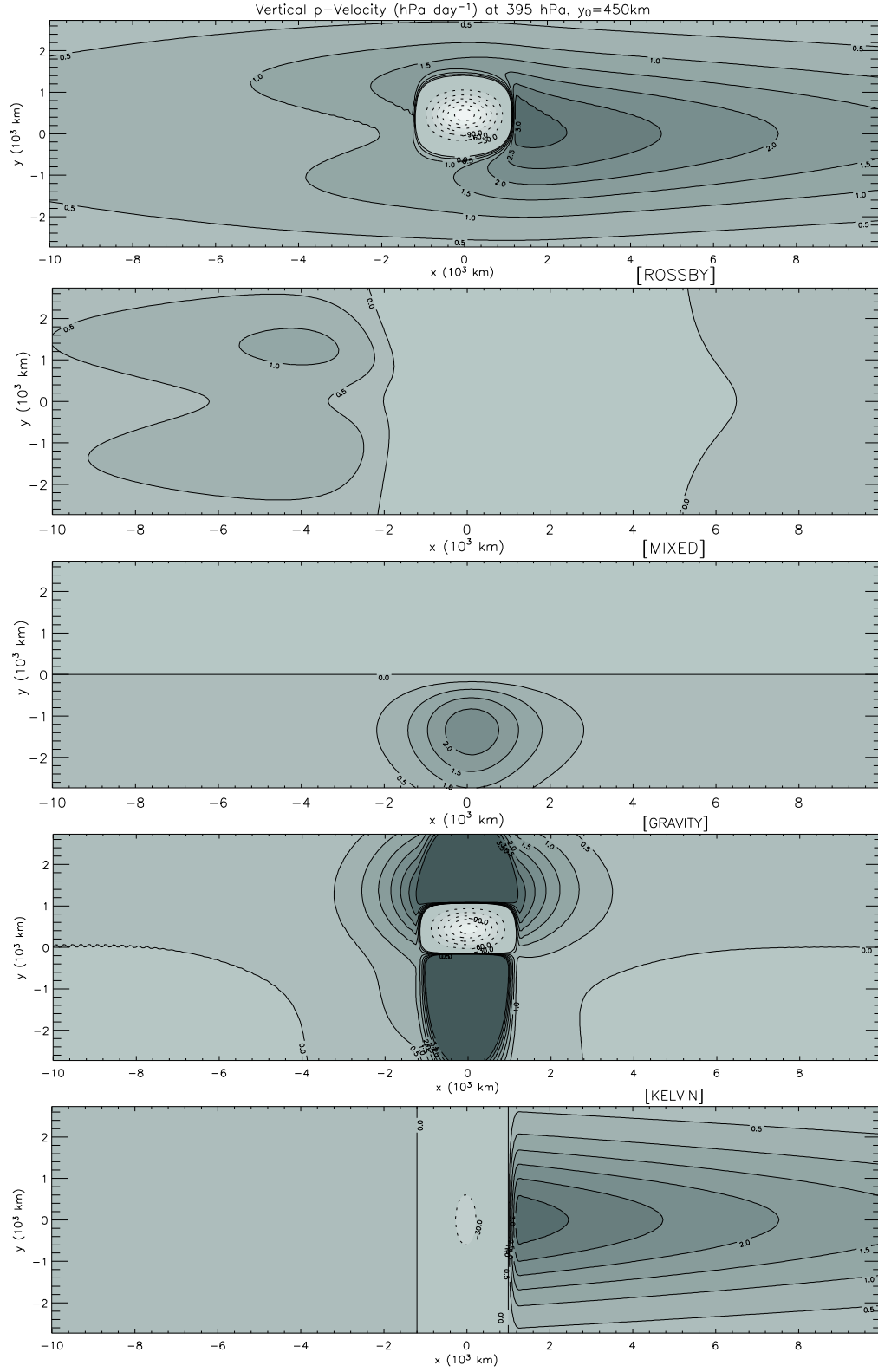
Figure 2.8: Same as Fig. 2.6, but the center of the convective forcing is shifted north of the equator ($y_0 = 450$ km), so the nonzero mixed Rossby-gravity component is shown as well.